ROYAL SOCIETY OF CHEMISTRY

RSC Advances

PAPER

View Article Online
View Journal | View Issue

Cite this: *RSC Adv.*, 2026, **16**, 28395

Exfoliation-free solvothermal synthesis of ink-like MoS_2 gel for printable water purification filters

Muralikrishna Sreeramareddygari, *[a] Jyothi Mannekote Shivanna, *[b] Zhoveta Yhobu, [c] S. Satyanarayana Reddy, [d] Mithran Somasundrum, [ae] Chatuporn Phanthong,[ae] Gurumurthy Hegde, [fgi] Patsamon Rijiravanich [ae] and Werasak Surareungchai[ah]

Received 10th February 2026
Accepted 18th May 2026

DOI: 10.1039/d6ra01189f

rsc.li/rsc-advances

A novel screen-printing approach was employed to fabricate molybdenum disulfide (MoS_2) based membranes using exfoliation-free solvothermally synthesized ink-like MoS_2 gel and Whatman filter paper (WFP). Three membranes, MoS_2-WFP-1, MoS_2-WFP-2, and MoS_2-WFP-3, were fabricated by varying the number of print coatings to tailor the hydrophobicity and mechanical integrity. Structural and morphological investigations were performed by X-ray Diffraction (XRD), X-ray Photoelectron Spectroscopy (XPS) and Field Emission Scanning Electron Microscopy (FE-SEM) analysis. The XPS results confirmed a well-adhered MoS_2 layer with mixed 1T/2H phases that enhanced mechanical and thermal stability. The MoS_2 incorporated membranes exhibited increased tensile strain, moderate water uptake (53–55%), and contact angles (104–118°) which increased with increasing coat number, demonstrating tunable surface wettability. In spite of reduced pure water flux, compared to bare filter paper, each coated membrane exhibited stable flux over a 60 min filtration period. The membranes efficiently removed the Congo red (~90%), methylene blue (~55%) and Cr(VI) (~72%) under pH-dependent conditions. The pH-dependent removal arises from electrostatic interactions between the MoS_2 surface and charged species, where protonation of the negatively charged MoS_2 surface at acidic pH enhances the attraction of anionic contaminants (Congo red and Cr anions such as such as $HCrO_4^-$ and $Cr_2O_7^{2-}$), while deprotonation at basic pH favors adsorption of cationic MB. The investigations confirm a simple, scalable and low-cost route for the fabrication of printable MoS_2 membrane filters suitable for wastewater purification.

1. Introduction

The removal of dyes and heavy metals from wastewater is crucial for environmental protection and public health. Membrane technology has emerged as an effective solution, offering efficient separation and purification processes with low energy consumption and mild operating conditions. Various types of membranes, including modified microfiltration,[1,2] nanofiltration,[3] ultrafiltration[4] and graphene oxide-based membranes,[5,6] have been developed to enhance pollutant removal efficiency. Graphene based membranes leverage high surface area and functionalization for effective separation of heavy metals and dyes, although their irregular pore structure can limit the efficiency.[7]

Molybdenum disulfide (MoS_2)-based membranes have shown potential in water treatment applications, enhancing ion and molecular separation processes. Their unique physiochemical properties and fabrication techniques contribute to improved efficiency and reduced energy consumption in water purification, as highlighted in research over the last few years.[8] MoS_2 nanosheets possesses high surface area, good chemical and thermal stability and offer easy surface functionalization. The membranes fabricated using MoS_2 nanosheets have exhibited superior water flux due to the hydrophilic nature of their edges and attain greater aqueous stability than that of graphene oxide or polymeric membranes.[9] Different

---

[a] *Sensor Technology Laboratory, Pilot Plant Development and Training Institute, King Mongkut's University of Technology Thonburi, Bangkhuntien-chaitalay Road, Thakam, Bangkok, 10150, Thailand. E-mail: sreerama.mur@kmutt.ac.th*

[b] *Department of Chemistry, Nitte Meenakshi Institute of Technology (NMIT), Nitte (Deemed to be University), Bengaluru, 560064, India. E-mail: jyothi0901@gmail.com*

[c] *Department of Chemical Sciences, Ariel University, Ariel 40 700, Israel*

[d] *Department of Physics, RV Institute of Technology and Management, Bengaluru, 560076, Karnataka, India*

[e] *Industrial Sensor Technology Research Team, National Center for Genetic Engineering and Biotechnology, National Science and Technology Development Agency at KMUTT (Bangkhuntien Campus), Bangkok, 10150, Thailand*

[f] *Dept of Chemistry, Christ University, Bangalore 560029, India*

[g] *Centre for Advanced Research and Development, Christ University, Bangalore 560029, India*

[h] *Faculty of Science, King Mongkut's University of Technology Thonburi, Pracha Uthit Rd, Thung Khru, Bangkok, 10140, Thailand*

[i] *Centre for Waste to Wealth Technology, Dayananda Sagar University, Devarakaggalahalli, Harohalli, Kanakapura Road, Bengaluru South Dt. – 562 112, India*

morphologies of MoS_2, such as nanoplatelets, enhance performance by creating more water channels, achieving up to 93% removal of heavy metals like Mn^{2+} and Zn^{2+}.[10] Incorporating MoS_2 into composite membranes can improve stability and separation efficiency, fostering advancements in membrane technology.[8]

The production of MoS_2 composite membranes at near-atomic thickness presents technological hurdles, yet this is crucial for maximizing their water treatment efficiency.[11] Chemical Vapour Deposition (CVD) and Atomic Layer Deposition (ALD) are widely employed measures to produce monolayer or sub-monolayer MoS_2 thin films. These methods offer continuous, high uniform and large-area MoS_2 nanosheets which are well aligned with the design and fabrication of MoS_2 membranes. However, these methods are limited for wider applications due to their complicated fabrication process. This could substantially increase the membrane production costs and limit industrial scale applications.[12] On the other hand, liquid exfoliation methods offer simple steps to produce MoS_2 nanosheets. The resulting nanosheets can be functionalized with other molecules, or polymers, to regulate the structure and function of the MoS_2. The resulting materials have been used for membrane fabrication through a simple vacuum filtration method.[13] Nonetheless, these methods are also limited in practical use due to low scalability and the necessity of Li^+ ions intercalation, which requires the use of hazardous solvents and an inert gas atmosphere.[14] Electrochemical intercalation or micromechanical exfoliation methods are still facing challenges to scale up, due to low yields.[15,16]

Interfacial polymerization, involving reaction on a porous substrate,[17] layer-by-layer assembly by sequential immersion cycles,[18] electrospray polymerization,[19] direct application of polymer on a support followed by phase inversion, and hybrid techniques such as electrospinning in combination with interfacial polymerization,[19] dip or spin coating of the nanomaterials onto the pre-formed layers,[20] are some of the other methods used for the fabrication of composite membranes to achieve thin but strong active layers on the supports. In one of our previous works, a scalable hydrothermal method was used for the production of defect rich MoS_2 nanosheets, to develop highly stable functionalized membranes. The MoS_2 membrane fabricated using pristine MoS_2 nanosheets showed poor aqueous stability whereas the MoS_2 nanosheets treated with trithiocyanuric acid (TTCA), prior to membrane fabrication through vacuum filtration, showed high aqueous stability and good heavy metal ion and molecular separation efficiency.[21] The defect rich MoS_2 nanosheets are functionalized and polymerized *via* thiol group containing TTCA, which greatly helped the strong adhesion onto the commercial Polyethersulfone (PES) membrane surface through hydrophobic π–π* stacking and electrostatic interactions between polythiocyanuric acid (PTCA) and PES. The fabricated membrane was able to remove dyes and heavy metals by ~80%.

Screen-printing technology offers several advantages including easy tailoring, economical, control over thickness, reproducibility, a wide substrate scope and easier scalability.[22] Screen-printing is a technology widely used in many industrial applications such as textiles, dye sensitized solar cells, silicon photovoltaics, printed electronics, sensors, snowboard graphics and medical devices.[23–25] This technology is also used in the fabrication of membranes such as PVA-based charged mosaic membranes to evaluate ion transport properties,[26] catalyst coated membranes in a proton exchange membrane fuel cells,[27] and so on. MoS_2 nanosheets are widely used for the fabrication of electrodes through screen printed technology to develop sensors, energy conversion and storage applications.[28–30] However, the screen-printed method has been rarely reported in fabrication of membranes for water purification processes.

Most membrane filtration experiments demand an applied pressure for the filtration process, and some membranes, even with pressure, suffer from insufficient permeate flux. Hence, the present work proposes the fabrication of MoS_2 membranes using ink-like MoS_2 gel on a regular Whatman grade 1 filter paper (WFP) *via* screen-printing methods. A solvothermal method was used to synthesise a ink-like MoS_2 gel suitable for screen-printing. This ink was screen-printed onto Whatman 1 filter papers to prepare MoS_2-WFP-1, MoS_2-WFP-2 and MoS_2-WFP-3 membranes, using 1, 2, and 3 screen-printing passes respectively, of the MoS_2 ink. The membranes were characterized using spectroscopic and microscopic methods. The water uptake, contact angle and mechanical properties of the fabricated membranes was investigated and the performance towards removal of dyes such as Congo red (CR), methylene blue (MB) and the heavy metal ion Cr(VI), at different pH conditions were also studied. This method enables the easy use of the fabricated membrane for water treatment applications, without the requirement of any specified membrane filtration units.

2. Materials and methods

2.1 Materials and reagents

All chemical reagents were used without further purification. De-ionized water was used throughout the experiments. Ammonium heptamolybatetetrahydrate, ethylene glycol, 1-octadecane, hexane, hydrochloric acid, potassium dichromate, Congo red, methylene blue and sodium hydroxide were purchased from the Merck. Trithiocyanuric acid was purchased from Tokyo Chemical Industry (TCI). Whatman filter paper grade 1 (pore size 11 μm and thickness 180 μm, Brand: Cytiva Whatman) was purchased from local suppliers.

2.2 Synthesis of MoS_2 ink

MoS_2 ink was synthesized as per our previous method with slight modifications.[31] In a typical reaction, 0.6179 g of ammonium heptamolybdate tetrahydrate was added to a 100 mL Teflon liner containing 60 mL of ethylene glycol and stirred vigorously at room temperature. Subsequently, 0.6204 g of trithiocyanuric acid was added as a sulfur source to the reaction mixture and stirred further to ensure homogeneity. Then, 10 mL of 1-octadecene was added to the reaction mixture and stirred for an additional 5 min. Then, the Teflon liner containing the reaction mixture was placed in a stainless-steel autoclave and maintained at 200 °C for 24 h. Subsequently, the autoclave was allowed to cool naturally and the resulting black-colored MoS_2 ink was washed thoroughly with hexane to remove 1-octadecene and unreacted compounds.

2.3 Fabrication of screen-printed filters using MoS_2 ink

Screen-printing technology was used for the fabrication of MoS_2 filters. A screen or fine mesh tightly stretched with a rigid frame is generally required for screen-printing. A mesh count of polyester 100 (open pore size 80) was used in this work for fabrication of the MoS_2 filters. Before printing, the undesired area of the mesh was masked out according to the desired printing sketch. The screen was then positioned over the Whatman number 1 filter paper and ink was applied to the screen, followed by swiping the ink through the screen, using a squeegee, from all the 4 sides (3 times from each side). The MoS_2 printed filter was dried at 60 °C in an electric oven. The resulting filter was placed in water for 12 h with occasional shaking to remove water soluble impurities. This filter is designated MoS_2-WFP-1. To increase the MoS_2 thickness, we repeated this process, to fabricate MoS_2-WFP-2, and repeated the process twice to fabricate MoS_2-WFP-3. A schematic diagram of MoS_2 screen-printing onto Whatman filter papers is shown in Scheme 1.

2.4 Instrumentation details

The XRD experiments were performed using a Bruker D8 Diffraction System with a Cu Kα source ($\lambda = 0.154178$ nm) and PANalytical monochromatic laboratory X-ray diffractometer ($\lambda = 1.5406$ Å). X-ray photoelectron spectroscopy (XPS) was analysed using a Kratos Axis Ultra DLD spectrometer with 165 mm hemispherical electron energy analyser. LabRam HR Evolution, Horiba, Japan Raman Spectrophotometer with LabSpec6 software was used to identify the phases of MoS_2. The surface morphology and element dispersive spectroscopy was investigated using Field Emission Scanning Electron Microscope (FE-SEM) (JEOL JSM-7100F, Singapore) and transmission electron microscopy (TEM) using TEM JEM-2100Plus. The surface roughness was quantified by Park NX10 Tapping mode Atomic Force Microscope (AFM) with a resonance frequency of 330 kHz. The AFM height images were presented after simple flattening using V 5.1.6XEI software. The size distribution and zeta potential of MoS_2 suspension (in water) was measured with a Zetasizer Nano ZS (Malvern Instruments), equipped with a 633 nm He–Ne laser. Glass cuvette and folded capillary cell were used for the analysis of size and zeta potential of MoS_2 ink. Surface area and pore volume of MoS_2 were analyzed by Belsorp mini II Brunauer–Emmett–Teller (BET) apparatus. Thermogravimetric analysis (TGA) of MoS_2 screen-printed Whatman filter papers was performed by using a Shimadzu Thermogravimetric Analyzer (model TGA-50). TGA analysis was carried out with a temperature ramp increasing at a rate of 10 °C min^{-1} in the range of 26 to 900 °C, under a nitrogen atmosphere. The mechanical strength of the fabricated membranes was tested using a Servo-hydraulic Fatigue Testing Machine, Walter + Bai–Series LEV-L, 25 kN, by preparing samples of dog bone shape. Bruker II alpha ATR Germany was used to analyse the Attenuated Total Reflectance-Infrared (ATR-IR) analysis.

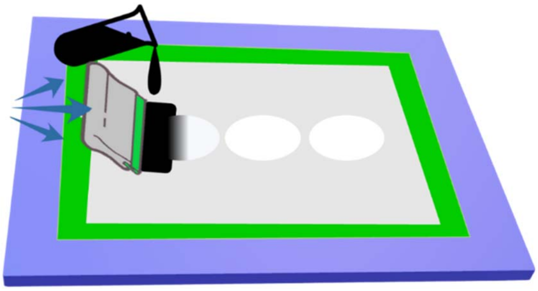

Scheme 1 Schematic representation of screen-printing for the fabrication of MoS_2 filters.

2.5 Membrane properties

The hydrophilicity of membranes is primarily evaluated through water uptake (WU) and contact angle (CA) measurements. To determine WU, three sets of 1 × 1 cm fabricated membrane samples (including prepared variants and a commercial Whatman 1) were immersed in water for 24 h. Dry weights (W_d) and equilibrium wet weights (W_w) were recorded, with percentage WU calculated using eqn (1)

$$\%\ \mathrm{WU} = \left(\frac{W_w}{W_d} - 1\right) \times 100 \tag{1}$$

This standardized gravimetric method ensures consistent evaluation of hydrophilic properties across different membrane formulations. The hydrophilic nature of the membrane surface was confirmed by contact angle measurements using a digital microscope and digital viewer.

The pure water flux (PWF) is another factor deciding the performance of the membrane. This was examined using a regular filtration unit of 1000 mL capacity, procured from Sigma Aldrich Pvt, Ltd. All water filtration experiments performed without applied pressure or without connection of vacuum pump. The volume of water permeated through membrane was measured every 10 min and the PWF (J_w, L m^{-2} h^{-1}) was calculated from eqn (2), by measuring the time, t, (in h), volume, V, of water (in L) and membrane area, A, (in m^2).

$$J_w = \frac{V}{A \times t} \tag{2}$$

2.6 Membrane performance

The performance of the membranes towards the removal of CR, MB and Cr(VI) was determined with respect to % rejection, and the permeate flux was evaluated using the above-mentioned filtration set up. The concentration of feed and permeate solutions was examined using a UV-visible spectrophotometer, wherein, for CR, MB and Cr(VI), the wavelengths used were 498, 664 and 370 nm, respectively. The % removal of the dyes and heavy metal ions was calculated using eqn (3)

$$\%\ \text{Removal} = \left(1 - \frac{C_t}{C_o}\right) \times 100 \tag{3}$$

where, C_o and C_t are the initial and final contaminant concentrations at time, t. The removal efficiency of MoS_2-WFP-1 was also examined at varied pH conditions. pH 4 for acidic, pH 7 for neutral and pH 9 for basic conditions, were maintained.

3. Results and discussions

MoS_2 ink was synthesized by a solvothermal method employing ethylene glycol and 1-octadecane as solvents, and ammonium heptamolybdate tetrahydrate and TTCA as Mo and S sources, respectively. TTCA is an organic molecule with three thiol groups, serving as multifunctional reagent. Its functions include acting as a reducing agent for the reduction of Mo^{6+} to Mo^{4+}, acting as a sulfur source for the formation of MoS_2, and forming the ink-like gel.[31] Ethylene glycol has a dual role as both reducing agent, and an intercalating agent for MoS_2.[32] 1-Octadecene was used as a polymerizing agent and also harnessed for reduction of the sulfur precursor.[33] The synthesized ink-like gel was suitable for the fabrication of printed materials through screen-printing technology.

Although the hydrothermal route is simple, reproducible, and suitable for laboratory-scale production, its direct translation to large-scale manufacturing is limited by autoclave volume, batch processing, and the difficulty of maintaining uniform heat and mass transfer at higher volumes. Therefore, the present work should be regarded as a laboratory-scale demonstration of a potentially scalable route and further work on larger reactors or continuous synthesis would be required to establish industrial scalability.

3.1 Characterizations

The fabrication of MoS_2 ink, screen-printed Whatman filter papers for water treatment involved synthesizing MoS_2 ink *via* a solvothermal method followed by deposition onto the Whatman filter paper using screen-printing technology. The resulting filters (MoS_2-WFP-1, MoS_2-WFP-2 and MoS_2-WFP-3) were initially tested for water purification. Among the three filters, MoS_2-WFP-1 exhibited slightly better properties in the majority of cases.

Therefore, only the MoS_2-WFP-1 was used for the spectroscopic and microscopic characterizations used to evaluate structural, chemical, thermal, and mechanical properties. The XRD patterns of WFP, MoS_2-WFP-1 and MoS_2 powder are provided in Fig. 1a and b. The WFP shows characteristic diffraction peaks at 2θ 14.6°, 16.2°, 22.38° and 33.8° which correspond to (110), (110), (200) and (004) diffraction planes of monolithic cellulose type I, respectively.[34] MoS_2 powder exhibits a dominant hexagonal 2H peak at 2θ 9.64° for reflecting (002) plane, which is corresponding to interlayer spacing of 0.92 nm. The downwards shift in (002) plane peak position from 14.13° to 9.64° demonstrates an enlarged interlayer spacing from 0.63 nm (JCPDS card 01-075-1539) to 0.92 nm, which was calculated based on Bragg's law ($2d\sin\theta = n\lambda$), which clearly suggests an expansion of the layered structure compared to conventional 2H MoS_2.[35] Additional peaks at 2θ, 32.7° and 57° reflecting (100) and (110) planes confirm in-plane crystallinity and layered stacking. Additionally, the broad nature of the peaks demonstrates the amorphous nature of the synthesized ink. In the case of MoS_2-WFP-1 (2θ at 9.64°), the absence of high-index diffraction peaks indicates short-range disorder within the nanocrystalline structure.[36] This arises due nanoflake fragmentation during screen-printing. The absence of the same is also attributed to the very low concentration of MoS_2 on the filter paper. The disordered configuration enhances active site density by exposing edge sulfur atoms, which are optimal for binding water contaminants like heavy metals. Also, the prominent cellulose peak and the less intense peaks of MoS_2 in MoS_2-WFP-1 confirms that the screen-printing process preserves the MoS_2 crystal structure while integrating it with the substrate. BET analysis was performed to find out the specific surface area and pore volume of the MoS_2. Fig. 1c displays the nitrogen adsorption–desorption isotherms of MoS_2. According to the IUPAC classification, the solvothermally synthesized MoS_2 exhibits a type-IV isotherm with a H3 type hysteresis loop, which indicates the characteristic of mesoporous materials. The attributed pores have presumably arisen due to the spaces between the cross-linked MoS_2 nanosheets which yield a large specific surface area. The average pore diameter and specific surface area of the MoS_2 are calculated to be 11.74 nm and 55.17 $m^2\ g^{-1}$, respectively. However, the BET pore diameter represents the intrinsic mesoporosity of the MoS_2 flakes, rather than the effective membrane filtration pore size, which is governed by the coated WFP architecture and interflake transport pathways.

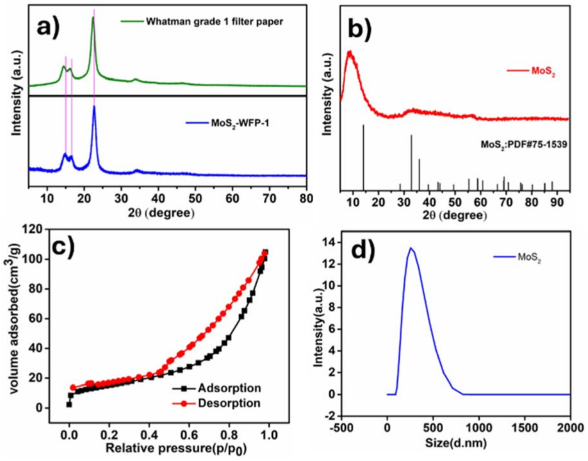

Fig. 1 XRD patterns of (a) WFP, and MoS_2-WFP-1 (b) MoS_2 (c) nitrogen adsorption–desorption isotherms of MoS_2 and (d) hydrodynamic size plot of MoS_2 dispersion analyzed by the DLS technique.

Fig. 1d represents the hydrodynamic size plot of solvothermally synthesized MoS_2 dispersion analyzed by the DLS technique corresponded to 300 nm. The zeta potential of MoS_2 was *ca.* −20.9 mV, which suggested that the synthesized MoS_2 has negatively charged surface (see Fig. S1 in SI).

To further understand the interaction between the substrate (WFP) and the prepared MoS_2 ink, the XPS spectra of MoS_2-

WFP-1 was investigated. The full scan survey spectrum along with deconvoluted Mo and S peaks are provided in Fig. 2a–d. Fig. 2a represents the wide-scan XPS survey spectrum of MoS_2-WFP-1 and displays prominent peaks corresponding to molybdenum (Mo), sulfur (S), carbon (C) and oxygen (O). The strong Mo and S signals confirm the presence of MoS_2, while the C and O peaks are attributed mainly to the cellulose substrate of the WFP and possible adventitious carbon. The high-resolution Mo 3d spectrum typically in the region between 224 to 237 eV (Fig. 2b), showed major peaks for Mo $3d_{5/2}$ and Mo $3d_{3/2}$ at 228.78 and 232.00 eV, respectively. These binding energies are characteristic of Mo^{4+} in the 1T phase of MoS_2 (48.7%, calculated based on peak area), indicating that the solvothermal synthesis and screen-printing process preserved the desired oxidation state and structure of molybdenum. The other pair of peaks at 230.04 and 232.91 eV corresponding to the 2H phase of MoS_2 (32.6%). The coexistence of 2H and 1T phases (as detected by XPS) is often beneficial, combining stability (2H) with reactivity (1T).[37] The peak at higher binding energies (235.63 eV for Mo^{6+}) indicates the presence of MoO_3 (7.7%) or other higher-valence states, which are usually observed in the synthesized MoS_2 by hydrothermal or solvothermal methods.[38–41] The presence of mixed phase MoS_2 was further confirmed by Raman analysis (Fig. 3). The other shoulder peak at 226.31 eV corresponding to the S 2s, due to emission from the defect-free regions of MoS_2 (11%).

Fig. 2c represents the high-resolution spectrum of S 2p. The two major peaks at 161.83 eV and 163.16 eV corresponding to the characteristic peaks of S^{2-} in MoS_2 which come from the majority of sulfur present in the desired sulfide state.[42] There are no significant peaks corresponding to oxidized sulfur species such as SO_4^{2-}, indicating no sulfur oxidation. The S : Mo atomic ratio, calculated from XPS data remains close to the ideal value of 2 : 1, further supporting the predominance of MoS_2. In Fig. 2a, the peak of C 1s at 284.8 eV, and O 1s at 532.2 eV, are attributed to the cellulose matrix of the WFP and the adsorbed MoS_2 species. The deconvoluted C 1s spectra confirms the 4 types of carbons bonds (Fig. 2d), C–C/C–H, C–O, C═O and O–C═O at 284.8, 286.25, 286.93 and 287.9 eV, respectively.[43] The significant C–O and O–C═O groups on the cellulose WFP surface provide abundant sites for hydrogen bonding[44] with sulfur atoms or oxygen-containing groups on MoS_2. The polar nature of the oxygenated carbon species increases the surface energy of the cellulose,[45] promoting better wetting and adhesion of the MoS_2 ink during screen printing. The preservation of the chemical structure of cellulose, as evidenced by C–C/C–H peak, ensures that the filter retains its fibrous, porous morphology, which physically entraps MoS_2 nanoflakes. The preservation of fibrous morphology was further confirmed by FESEM images.

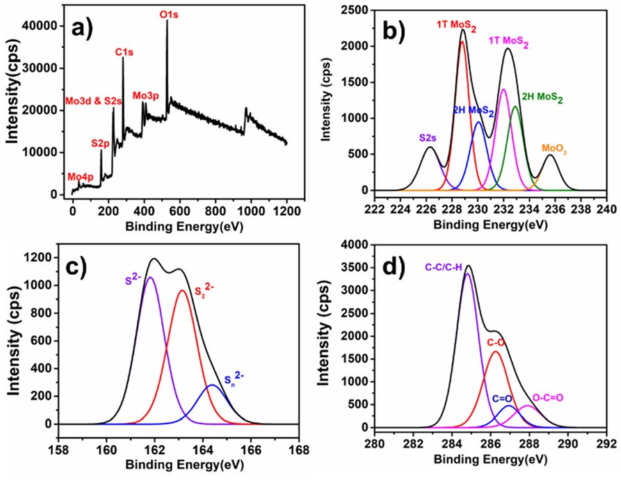

Fig. 2 XPS binding energy peaks for MoS_2-WFP-1 (a) full scan; (b) high resolution binding energy peaks for Mo; (c) high resolution binding energy peaks for S and (d) high resolution binding energy peaks for C.

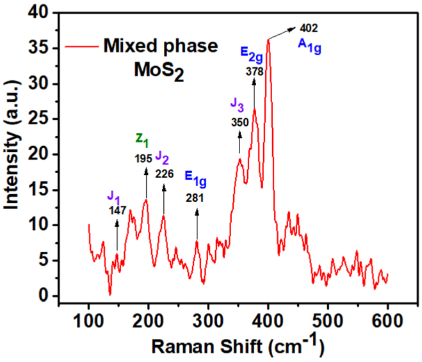

Fig. 3 Raman shifts for MoS_2-WFP-1.

The Raman spectrum shown in Fig. 3 confirms the successful formation of mixed-phase MoS_2 containing both 1T and 2H phase. The co-existence of these phases is evidenced by the appearance of characteristic vibrational modes corresponding to both crystal structures. The two prominent peaks at approximately 378 and 402 cm^{-1} correspond to the characteristic Raman-active modes of 2H–MoS_2. The peak at 378 cm^{-1} is assigned to the in-plane E^1_{2g} mode, arising from the opposite in-plane vibrations of Mo and S atoms, while the peak at 402 cm^{-1} corresponds to the out-of-plane A_{1g} mode, mainly associated with sulphur atom vibrations perpendicular to the MoS_2 layers. In addition to these peaks, the characteristic of 1T phase peaks are observed at low frequency range referring to J1, J2 and J3 modes.[46] These J peaks are presumed to originate from symmetry lowering and structural rearrangement from the stable 2H phase to the metastable metallic 1T phase.

The FESEM micrographs of WFP and MoS_2-WFP-1 are provided in Fig. 4a and b. The fine fibrous and porous morphology for pristine WFP is observed in Fig. 4a. The cellulose fibers, typically measuring micrometers in diameter, are randomly interwoven, creating a three-dimensional matrix with interconnected pores. This structure is ideal for filtration, allowing for high water permeability and providing a large surface area for subsequent functionalization. With the screen-printing of prepared MoS_2 ink on WFP (Fig. 4b and b(1)), the cellulose fibers were coated with a continuous, conformal layer of MoS_2 nanoflakes. The coating appears as a textured sheath

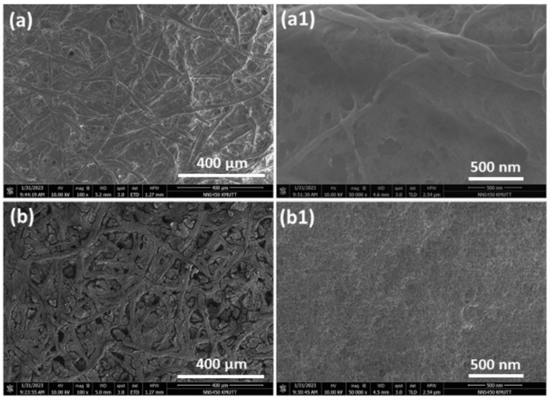

Fig. 4 FESEM images of (a) and (a1) WFP; (b) and (b1) MoS_2-WFP-1.

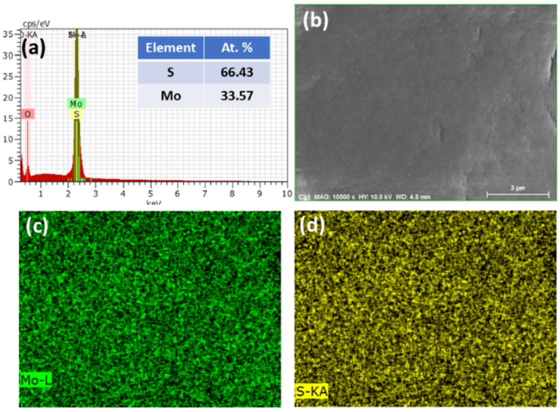

Fig. 6 (a) Elemental composition; (b) respective FESEM image; (c) and (d) elemental mapping for Mo and S, respectively for MoS_2-WFP-1.

enveloping the fibers, indicating strong adhesion and effective coverage. At higher magnification, the MoS_2 layer is composed of overlapping, plate-like nanoflakes of nanometer dimensions.

The surface of the coated fibers is significantly rougher than that of the bare cellulose, due to stacking of MoS_2 nanosheets. The increased roughness of WFP after screen printing of MoS_2 is supplemented by AFM analysis and the images are provided in Fig. 5. The pristine WFP presented smoother surface compared to the MoS_2 screen printed one. The appearance of pronounced ridges, valleys, and aggregated domains for the MoS_2 printed membrane clearly indicated the increased roughness. The average roughness of WFP and MoS_2-WFP-1, measured at 5 different positions is found to be 19.53 and 30.25 nm, respectively, which clearly quantifies the increased surface roughness. This roughness increases the effective surface area, which is beneficial for adsorption and catalytic applications.

Along with the morphology, EDX mapping was performed to confirm the presence and atomic ratio of Mo and S in MoS_2-WFP-1. The results are displayed in Fig. 6. The atomic percentage for Mo and S are 33.57 and 66.43%, respectively, which is expected for MoS_2. The mapping showed the distribution of Mo and S throughout the WFP surface indicating the uniformity of the surface.

Following the examination of surface morphology, the study was extended to analyze the mechanical and thermal stabilities of the prepared membranes. The thermo-gravimetric analysis performed for WFP and MoS_2-WFP-1 is given in Fig. 7a, and stress *vs.* strain graphs predicting mechanical strengths for all the membranes are provided in Fig. 7b. For the WFP membrane, a sharp weight loss begins around 310 °C, corresponding to the rapid decomposition of the cellulose. Complete degradation occurs before 400 °C, with minimal residual mass, which indicates thermal stability. For the MoS_2 printed filter, the initial thermal decomposition started at a similar temperature as that of WFP, but progressed more gradually than the uncoated paper. The residual mass remaining even after 800 °C (around 12%) is attributed to a thermally stable MoS_2 phase.

The presence of MoS_2 on WFP, delayed the onset of degradation and reduced the rate of mass loss. The stress–strain behavior of the fabricated membranes under tensile loading were investigated. The WFP membrane exhibited a higher initial stress response, but broke at a relatively low strain (0.67%). The curve showed a sharp drop after the peak, indicating the brittle fracture, which is typical for unsupplemented cellulose networks. With increased number of prints of MoS_2 on the WFP, the strain at break increased to 0.84, 1.13 and 1.18%, with increasing prints of MoS_2. Along with increased stress at peak, it is also observed that, the ductile and tough nature of the fabricated membranes also enhanced. The MoS_2 filling the cellulose matrix could bridge the gaps between the cellulose fibers, which could distribute the stress more evenly and prevent premature fiber fracture and hence the increased ductile nature. It is also noted that, with an increasing number of prints (layers), the strain-at-break increases, confirming that the nanocoating directly reinforces the fibrous matrix. The enhanced thermal as well as mechanical stability of WFP

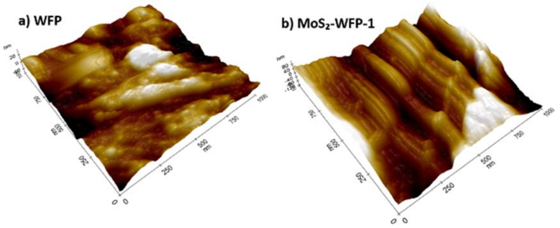

Fig. 5 AFM images of (a) WFP and (b) MoS_2-WFFP-1.

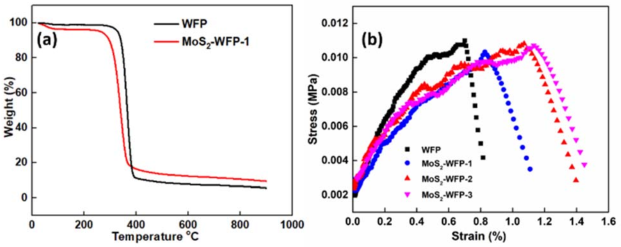

Fig. 7 (a) TGA curves for WFP and MoS_2-WFP-1; (b) stress *vs.* strain curves for all fabricated membranes along with WFP.

membranes with MoS_2 coating is advantageous for the regeneration of the membrane as well as usage of membranes for long-term water treatment, when compared to the bare WFP membrane.

3.2 Membrane performance

For water treatment applications, membrane design should aim for an optimal sufficient flux and effective contaminant removal. The PWF of WFP and MoS_2 coated membranes is provided in Fig. 8. The WFP without any coating presented a highest PWF of ∼40–43 L m^{-2} h^{-1} across the test period of 60 min. MoS_2-WFP-1, MoS_2-WFP-2 and MoS_2-WFP-3 showed approximately 35–37, 31–33 and 28–33 L m^{-2} h^{-1}, respectively. The results indicate that with increasing MoS_2 loading (number of coats), the PWF reduced. Nevertheless, the flux remained stable over the time, indicating good structural integrity and minimal compaction. The progressive decrease in the PWF from WFP to MoS_2-WFP-3 is attributed to the sequential deposition of MoS_2, which partially occlude the pores of the cellulose matrix. As the MoS_2 layer thickens, the effective pore size decreases and the hydraulic resistance increases, leading to lower water permeability.

Reported pure water fluxes for MoS_2-based membranes vary widely depending on fabrication method, thickness, and support material. For example, MoS_2/GO composite membranes have shown fluxes from 8.8 to 48.3 L m^{-2} h^{-1}, while pure MoS_2 nanosheet membranes can achieve 30–250 L m^{-2} h^{-1} bar^{-1} under pressure-driven conditions.[47–49] The values observed here for screen-printed MoS_2-WFP membranes are consistent with these reports, especially considering the absence of external pressure in gravity-driven filtration.

Along with PWF, water uptake studies were also performed to understand the water absorption ability of the fabricated membranes. The results are provided in Fig. 8b. The WFP membrane presented a WU of 49.6% (mean) and for MoS_2 coated membranes, the WU increased to 53.5 to 55.5%. Despite increased hydrophobicity, the WU remained almost same. This indicates that, MoS_2 layers, while making the surface hydrophobic, did not fully prevent bulk water adsorption. This could be due to the retention of hydrophilic sites by cellulose and the access provided by the porous structure. The measured average contact angles for WFP, MoS_2-WFP-1, MoS_2-WFP-2 and MoS_2-WFP-3 are of 25.9, 104.7, 108.6 and 118.1°, respectively (the photographs are presented in Fig. 6b). When compared to WFP membranes, MoS_2-coated membranes showed a dramatic rise in CA to above 100°, thus demonstrating increased hydrophobicity, as MoS_2 nanoflakes were layered. With increased print layers, the CA further increased, but the changes were insignificant. Despite enhanced surface hydrophobicity with respect to increased number of prints or coats, the bulk water uptake remained high. This is due to water absorption driven by internal hydrophilic cellulose, as well as the surface. Moderate porosity was preserved within the cellulose matrix even after 3 coats of MoS_2, hence, obtaining the PWF and water uptake.

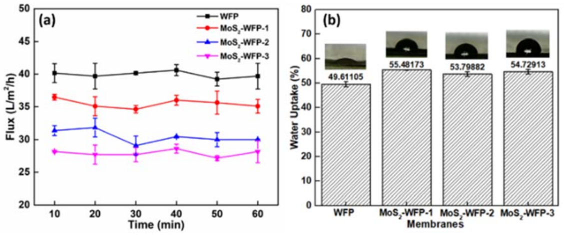

Fig. 8 (a) Pure water flux; (b) water uptake for WFP, MoS_2-WFP-1, MoS_2-WFP-2 and MoS_2-WFP-3 membranes.

3.3 Removal of water contaminants

To investigate the practical applications of the fabricated membranes, cationic methylene blue dye (MB), anionic Congo red dye (CR) and the toxic metal ion Cr(VI), were selected. The permeate flux and contaminant removal percentage for all the membranes, for each contaminant was investigated. The MoS_2-WFP-1 membrane was also investigated at different pH values. The results with respect to removal of MB, CR and Cr(VI) are provided in Fig. 9–11, respectively. For all the three contaminants, Fig. 9a, 10a and 11a, shown that the permeate flux followed a similar trend. The uncoated WFP membrane exhibited the greatest flux, varying from ∼42 to 47 L m^{-2} h^{-1}. Successive MoS_2 coatings caused a decrease in flux. For the single coating, MoS_2-WFP-1, 36–37 L m^{-2} h^{-1} of flux was obtained. This lowered to ∼28 to 30 L m^{-2} h^{-1} for MoS_2-WFP-3 membrane (3 coats of MoS_2). Additional MoS_2 layers fill surface microvoids and reduce effective pore size, leading to greater hydraulic resistance. Despite this, all the membranes maintained substantial flux, indicating they preserved macro-porosity. The trend was consistent across all the tested contaminants. Hence, the effect of increased MoS_2 coatings was independent of the nature of the contaminants. The removal percentages of respective contaminants, at neutral pH (without altering) are shown in Fig. 9b, 10b and 11b.

Fig. 9c, 10c and 11c present the permeate flux at different pH and demonstrate a generally stable flux, with only minor

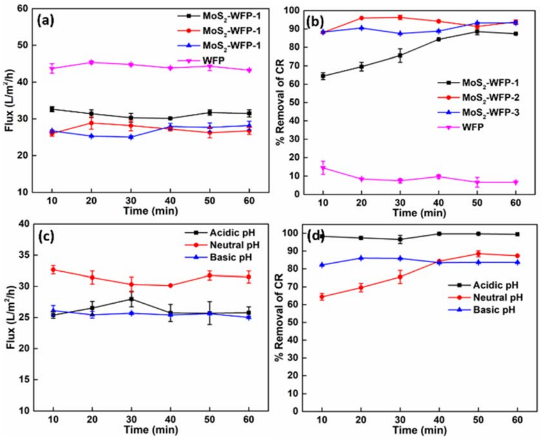

Fig. 9 (a) Permeate flux *vs.* time; (b) % removal of CR *vs.* time graphs for the membranes with and without MoS_2 prints on WFP; (c) flux at different pH conditions *vs.* time; (d) % removal of CR at different pH conditions *vs.* time graphs for the membrane MoS_2-WFP-1.

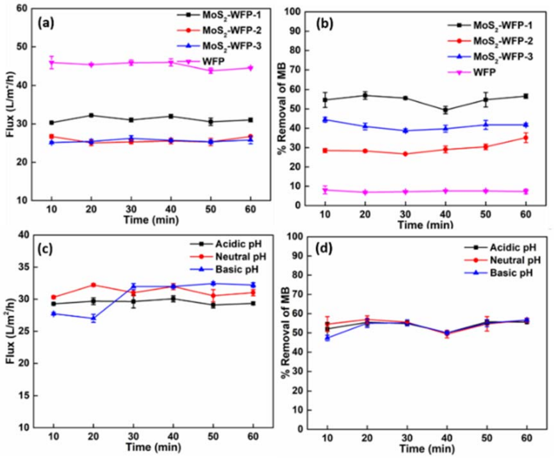

Fig. 10 (a) Flux *vs.* time; (b) % removal of MB *vs.* time graphs for the membranes with and without MoS_2 prints on WFP; (c) flux in different pH conditions *vs.* time; (d) % removal of MB at different pH conditions *vs.* time graphs for the membrane MoS_2-WFP-1.

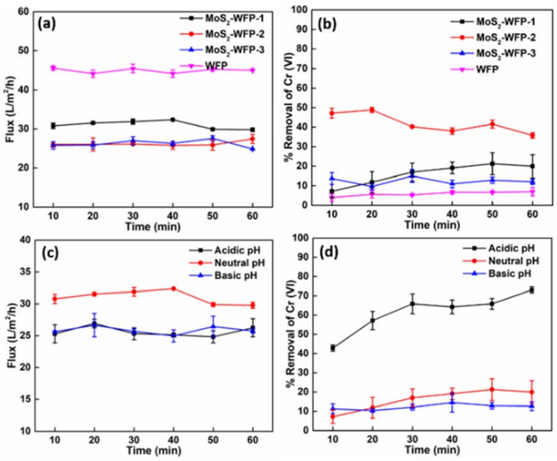

Fig. 11 (a) Flux *vs.* time; (b) % removal of Cr(VI) *vs.* time graphs for the membranes with and without MoS_2 prints on WFP; (c) flux in different pH conditions *vs.* time; (d) % removal of Cr(VI) at different pH conditions *vs.* time graphs for the membrane MoS_2-WFP-1.

fluctuations. A slight flux decrease at extreme pH conditions suggests minor swelling, or interactions between the membranes and solution components, but overall, the flux was maintained. This indicates the good chemical robustness of the membranes. The removal efficiency of the MoS_2-WFP-1 membrane towards CR, MB and Cr(VI) at different pH conditions is provided in Fig. 9d, 10d and 11d, respectively. For a better understanding of the mechanism involved, the zeta potentials of all three considered contaminants at varied pH was measured and the results are provided in SI as Table S1 and Fig. S2 to S10.

CR, being an anionic dye, was removed by ∼90.3% at acidic pH and the removal then dropped to ∼63% in basic pH (Fig. 9d). At acidic pH, the negative MoS_2 surface (zeta potential −20.9 mV) is protonated and is therefore expected to favor electrostatic attraction toward the anionic CR. The zeta potential of CR becomes increasingly negative with increasing pH (−40.8 mV at pH 4 to −65.5 mV at pH 9), removal efficiency decreased correspondingly. Since both the membrane and CR possess negative surface charges, stronger electrostatic repulsion at higher pH reduces rejection efficiency. The comparatively higher removal at pH 4 may be attributed to weaker electrostatic repulsion.

In the case of MB, the dye exhibits a positive zeta potential at pH 4 (+16.0 mV), resulting in strong electrostatic attraction toward the negatively charged membrane and enhanced removal behaviour. As the pH increases, the zeta potential becomes slightly negative (−7.37 to −9.41 mV), reducing attractive interactions. Nevertheless, moderate rejection is still observed, likely due to adsorption and steric hindrance effects.

For Cr species, the zeta potential remains negative across the investigated pH range. The maximum removal of about 72% (Fig. 11d) was achieved at a lower pH for Cr(VI), owing to the anionic forms of Cr(VI), such as $HCrO_4^-$ and $Cr_2O_7^{2-}$. At low pH, the protonated, positively charged MoS_2 surface strongly attracts these anions. Reductive adsorption (and possible partial reduction to Cr(III)) is also favored under acidic conditions. Overall, the work validates MoS_2 ink printing as a green, low-cost route to fabricate high-strength, reusable nanocomposite paper membranes, establishing a foundation for future scaling, and optimization towards heavy metal and organic contaminant remediation systems.

3.4 Leaching studies

Leaching of MoS_2 nanosheets from the WFP over a period of time could be a major issue. To evaluate its stability at laboratory level, dilute acid (0.1 N HCl) was allowed to pass through the membrane for about 16 h, washed with a distilled water, dried at 60 °C in oven for 8 hours and the ATR-IR before and after the treatment were measured and the results are provided in Fig. 12. The pristine WFP spectrum exhibits characteristic cellulose adsorption bands. The broad band around 3200 to 3400 cm^{-1} is attributed to the O–H stretching vibrations, while the peaks near 2929 cm^{-1} correspond to C–H stretching vibrations. The bands seen at 1420–1450 cm^{-1} and 1320–1360 cm^{-1}

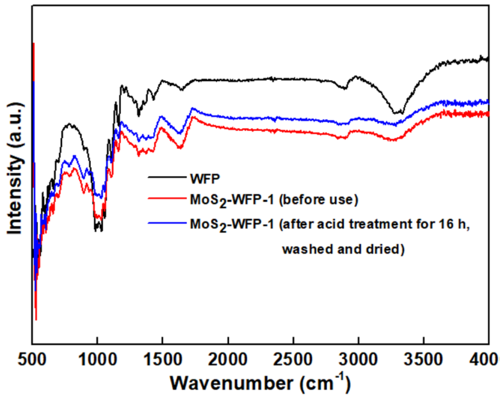

Fig. 12 ATR-IR spectra of WFP, MoS_2-WFP-1 (before use) and MoS_2-WFP-1 (after acid treatment for 16 h).

are associated with CH_2 bending and O–H deformation vibrations of cellulose. Additionally, the intense band near 1050–1100 cm^{-1} is assigned to C–O–C and C–O stretching vibrations of the polysaccharide backbone.[50]

After MoS_2 coating, noticeable changes in spectral intensity and band profile are observed for MoS_2-WFP-1, confirming successful deposition of the MoS_2 layer over the cellulose substrate. The reduction in intensity of cellulose-related bands suggests partial surface coverage of the WFP fibers by MoS_2 sheets. Slight broadening and suppression of the hydroxyl and C–O vibration bands further indicate interfacial interactions between the MoS_2 coating and cellulose network.

The ATR-IR spectrum of the membrane after immersion in dilute acid and subsequent washing remains highly similar to that of the membrane before use. Minor intensity variations observed after washing may arise from partial removal of loosely attached particles. However, the absence of significant spectral alterations confirms that the membrane structure remains largely intact and the coated layer maintains good adhesion to the WFP substrate even after chemical exposure and washing treatment.

4. Conclusions

The study demonstrated a novel, scalable screen-printing strategy for the fabrication of MoS_2 based filtration membranes derived from solvothermally synthesized MoS_2 ink and Whatman filter paper. Structural and spectroscopic characterizations confirmed the coexistence of 1T and 2H MoS_2 phases, uniform nanoflake coverage and strong MoS_2 cellulose interfacial adhesion, ensuring thermal stability. Hydrophilicity and porosity could be effectively modulated with successive print layers: while surface hydrophobicity increased three-fold compared to the bare filter paper, efficient water uptake and permeability were maintained due to the hydrophilic cellulose network. The screen-printed MoS_2 membranes exhibited notable contaminant removal performance, achieving up to 90% Congo red, 55% methylene blue, and 72% Cr(VI) removal through synergistic adsorption and electrostatic interaction mechanisms. The pH-dependent removal trends indicated tunable selectivity, with acidic conditions favoring anionic pollutant removal and basic conditions contributing to cationic dye elimination. Compared to conventional nanofiltration membranes, the MoS_2-printed filters achieve competitive water flux and selectivity without requiring applied pressure, representing a cost-efficient, sustainable alternative for decentralized water treatment. In addition, no leaching of MoS_2 is observed after treating the study membrane with dilute acid, followed by washing and drying process, as confirmed by ATR-IR, suggests the potential of a membrane to be taken forward for large scale applications. However, the extensive studies on stability as well as scalability remain as the future scope of this work.

Author contributions

Muralikrishna Sreeramareddygari: conceptualization, methodology, analysis, writing – original draft, editing, funding acquisition,. Jyothi Mannekote Shivanna: analysis, investigation and writing – original draft preparation, editing, supervision. Zhoveta Yhobu: visualization, investigation. Satyanarayana Reddy: analysis. Mithran Somasundrum: reviewing. Chatuporn Phanthon: data curation. Gurumurthy Hegde: reviewing and analysis. Patsamon Rijiravanich: analysis and reviewing. Werasak Surareungchai: data curation, visualization.

Conflicts of interest

There are no conflicts to declare.

Data availability

Data is available with the relevant request to the authors.

Supplementary information (SI): the zeta potential plots of MoS_2 and all three contaminants under different pH conditions. See DOI: https://doi.org/10.1039/d6ra01189f.

Acknowledgements

This research project is supported by King Mongkut's University of Technology Thonburi (KMUTT), Thailand Science Research and Innovation (TSRI), and National Science, Research and Innovation Fund (NSRF) Fiscal year 2025 Grant number: FRB680074/0164. The authors would like to acknowledge the Department of Chemistry, NMIT, for providing Seed money to carryout part of the work. We extend our gratitude to Mr Wachira Chaiworn for his help with the screen-printing of MoS_2 membranes.

References

1 R. Yu, H. Wang, R. Wang, P. Zhao, Y. Chen, G. Liu and X. Liao, *Water Res.*, 2022, **218**, 118469.

2 D. Wanke, A. da Silva and C. Costa, *Chem. Eng. Res. Des.*, 2021, **171**, 268–276.

3 M. Jyothi, K. Soontarapa, M. Padaki, R. G. Balakrishna and A. M. Isloor, *J. Membr. Sci.*, 2017, **533**, 229–240.

4 M. Jyothi, V. Nayak, M. Padaki and R. G. Balakrishna, *J. Photochem. Photobiol., A*, 2017, **339**, 89–94.

5 Y. Wei, Y. Zhang, X. Gao, Z. Ma, X. Wang and C. Gao, *Carbon*, 2018, **139**, 964–981.

6 F. Jia, X. Xiao, A. Nashalian, S. Shen, L. Yang, Z. Han, H. Qu, T. Wang, Z. Ye and Z. Zhu, *Nano Res.*, 2022, **15**, 6636–6654.

7 F. A. Janjhi, D. Janwery, I. Chandio, S. Ullah, F. Rehman, A. A. Memon, J. Hakami, F. Khan, G. Boczkaj and K. H. Thebo, *ChemBioEng Rev.*, 2022, **9**, 574–590.

8 F. A. Janjhi, I. Chandio, D. Janwery, A. A. Memon, K. H. Thebo, G. Boczkaj, V. Vatanpour and R. Castro-Muñoz, *Chem. Eng. Res. Des.*, 2023, **199**, 327–347.

9 M. Sreeramareddygari, J. M. Shivanna, M. Somasundrum, K. Soontarapa and W. Surareungchai, *Chem. Eng. J.*, 2021, **425**, 130592.

10 D. E. Al Momani, F. Arshad, I. Taha, D. H. Anjum and L. Zou, *npj Clean Water*, 2024, **7**, 64.

11 P. O. Oviroh, T.-C. Jen, J. Ren and A. van Duin, *npj Clean Water*, 2023, **6**, 14.

12 N. Sun, C. Gu, H. Ji, X. Zhu, X. Liu, Y. Zhuang and L. Wang, *Desalination*, 2024, **575**, 117270.

13 L. Ries, E. Petit, T. Michel, C. C. Diogo, C. Gervais, C. Salameh, M. Bechelany, S. Balme, P. Miele and N. Onofrio, *Nat. Mater.*, 2019, **18**, 1112–1117.

14 D. Saha and P. Kruse, *J. Electrochem. Soc.*, 2020, **167**, 126517.

15 A. Ejigu, I. A. Kinloch, E. Prestat and R. A. Dryfe, *J. Mater. Chem. A*, 2017, **5**, 11316–11330.

16 Y. Li, X. Yin and W. Wu, *Ind. Eng. Chem. Res.*, 2018, **57**, 2838–2846.

17 E. A. M. Saleh, A. Kumar, T. Alghazali, S. Ganesan, A. Shankhyan, G. C. Sharma, K. S. Naidu and M. Rahbari-Sisakht, *Environ. Sci.:Water Res. Technol.*, 2025, **11**, 1059–1085.

18 T. Zhu, Q. Xia, J. Zuo, S. Liu, X. Yu and Y. Wang, *Adv. Membr.*, 2021, **1**, 100008.

19 Q. Zhang, R. Zhou, X. Peng, N. Li and Z. Dai, *Polymers*, 2023, **15**, 3290.

20 B. S. Lalia, V. Kochkodan, R. Hashaikeh and N. Hilal, *Desalination*, 2013, **326**, 77–95.

21 M. Sreeramareddygari, J. Mannekote Shivanna, M. Somasundrum, K. Soontarapa and W. Surareungchai, *Chem. Eng. J.*, 2021, **425**, 130592.

22 M. Fekete, R. K. Hocking, S. L. Chang, C. Italiano, A. F. Patti, F. Arena and L. Spiccia, *Energy Environ. Sci.*, 2013, **6**, 2222–2232.

23 T. A. Sherazi, in *Encyclopedia of Membranes*, Springer, 2016, pp. 1753–1754.

24 C. Chen, C. Ran, Q. Yao, J. Wang, C. Guo, L. Gu, H. Han, X. Wang, L. Chao and Y. Xia, *Advanced Science*, 2023, **10**, 2303992.

25 A. G.-M. Ferrari, S. J. Rowley-Neale and C. E. Banks, *Talanta Open*, 2021, **3**, 100032.

26 M. Higa, A. Jikihara, T. Maeda, S. Morinaga, Y. Kakihana and M. Higa, *J. Membr. Sci.*, 2024, **711**, 123158.

27 W. Wang, S. Chen, J. Li and W. Wang, *Int. J. Hydrogen Energy*, 2015, **40**, 4649–4658.

28 S. J. Rowley-Neale, G. C. Smith and C. E. Banks, *ACS Appl. Mater. Interfaces*, 2017, **9**, 22539–22548.

29 M. Pavličková, L. Lorencová, M. Hatala, M. Kováč, J. Tkáč and P. Gemeiner, *Sci. Rep.*, 2022, **12**, 11900.

30 R. Chaturvedi, R. Pandey, S. Singhania and A. Garg, *Electrochim. Acta*, 2025, 147090.

31 Z. Yhobu, M. Sreeramareddygari, C. Phanthong, S. Budagumpi, D. H. Nagaraju, W. Chaiworn, M. Somasundrum, P. Rijiravanich, S. Chuangchote and W. Surareungchai, *Int. J. Hydrogen Energy*, 2025, **139**, 247–256.

32 S. Palencia-Ruiz, D. Uzio, C. Legens, D. Laurenti and P. Afanasiev, *Appl. Catal., A*, 2021, **626**, 118355.

33 E. Dhaene, J. Billet, E. Bennett, I. Van Driessche and J. De Roo, *Nano Lett.*, 2019, **19**, 7411–7417.

34 M. Verma, T. K. Naqvi, S. K. Tripathi, M. M. Kulkarni, N. E. Prasad and P. K. Dwivedi, *IEEE Trans. NanoBiosci.*, 2021, **21**, 294–300.

35 G. Tontini, G. D. L. Semione, C. Bernardi, R. Binder, J. D. B. de Mello and V. Drago, *Ind. Lubr. Tribol.*, 2016, **68**, 658–664.

36 J. Xie, J. Zhang, S. Li, F. Grote, X. Zhang, H. Zhang, R. Wang, Y. Lei, B. Pan and Y. Xie, *J. Am. Chem. Soc.*, 2013, **135**, 17881–17888.

37 M. Chhowalla, H. S. Shin, G. Eda, L.-J. Li, K. P. Loh and H. Zhang, *Nat. Chem.*, 2013, **5**, 263–275.

38 M. Sreeramareddygari, M. Somasundrum and W. Surareungchai, *New J. Chem.*, 2020, **44**, 5809–5818.

39 J. Yu, D. Ma, L. Mei, Q. Gao, W. Yin, X. Zhang, L. Yan, Z. Gu, X. Ma and Y. Zhao, *J. Mater. Chem. B*, 2018, **6**, 487–498.

40 M. S. Fuhrer and J. Hone, *Nat. Nanotechnol.*, 2013, **8**, 146–147.

41 H. Shi, R. Yan, S. Bertolazzi, J. Brivio, B. Gao, A. Kis, D. Jena, H. G. Xing and L. Huang, *ACS Nano*, 2013, **7**, 1072–1080.

42 S. Heo, Y. Ishiguro, R. Hayakawa, T. Chikyow and Y. Wakayama, *APL Mater.*, 2016, **4**, 030901.

43 S. K. Das, C. Dickinson, F. Lafir, D. F. Brougham and E. Marsili, *Green Chem.*, 2012, **14**, 1322–1334.

44 M. Wohlert, T. Benselfelt, L. Wågberg, I. Furó, L. A. Berglund and J. Wohlert, *Cellulose*, 2022, **29**, 1–23.

45 B. Lindman, B. Medronho, L. Alves, C. Costa, H. Edlund and M. Norgren, *Phys. Chem. Chem. Phys.*, 2017, **19**, 23704–23718.

46 S. Das, G. Swain and K. Parida, *Mater. Chem. Front.*, 2021, **5**, 2143–2172.

47 J. Ma, X. Tang, Y. He, Y. Fan and J. Chen, HaoYu, *Desalination*, 2020, **480**, 114328.

48 Z. Wang, Q. Tu, S. Zheng, J. J. Urban, S. Li and B. Mi, *Nano Lett.*, 2017, **17**, 7289–7298.

49 Z. Wang, Q. Tu, S. Zheng, J. J. Urban, S. Li and B. Mi, *Nano Lett.*, 2017, **17**, 7289–7298.

50 K. Zhang, M. Wang, M. Wu, Q. Wu, J. Liu, J. Yang and J. Zhang, *Cellulose*, 2020, **27**, 469–480.